

# Paper NA

Pierre

February 17, 2017

## 1 Introduction

The North American continent consists of an ancient cratonic core, formed during the Archean that has not been subjected to orogeny for at least 1.8 Ga, bordered to the southeast, by progressively younger, stable, Proterozoic provinces (Hoffman 1988). In the west, the Rocky Mountain Front (RMF) separates the Proterozoic and Archean shield from younger, tectonically active provinces (Fig. 1). This relatively regular configuration makes North America an ideal target for seismic tomography, to investigate the relationship of lithospheric and asthenospheric structure to the geological features observed at the surface.

Differences in the seismic velocity structure between the craton and the western US extending down to at least 200 km were established already in the 1960's and 70's from the first studies of teleseismic P and S wave travel time anomalies (e.g. Cleary and Hales 1966, Herrin and Taggart 1968, Poupinet 1979), the first tomographic images based on P and S travel times (Romanowicz 1979) and long period surface waveforms (Woodhouse and Dziewonski 1984), as well as contrasted velocity-depth profiles obtained from the modeling of shear body waveforms at relatively short distances (e.g. Grand and Helmberger 1984).

More recent shear wave tomography, at scales from global (e.g. Su et al. 1994, Mégnin and Romanowicz 2000, Shapiro and Ritzwoller 2002, Panning and Romanowicz 2006, Kustowski et al. 2008, Ritsema et al. 2010, Lekić and Romanowicz 2011, Debayle and Ricard 2012, Schaeffer and Lebedev 2013) to continental (van der Lee and Frederiksen 2005, Yuan et al. 2011; 2014, Schaeffer and Lebedev 2014), confirm the presence of strong lateral variations in the thickness of the lithosphere across the RMF, with lithospheric roots extending down to 200-250 km under the craton, thinning abruptly to the west to less than 80-100 km. This is also found from azimuthal anisotropy tomography, where it is manifested by a change in the anisotropy fast axis

direction across the lithosphere-asthenosphere boundary (LAB) (Marone and Romanowicz 2007, Yuan and Romanowicz 2010).

While the mechanism of craton formation is still widely debated (e.g. King 2005, Lee et al. 2011), the presence of finer scale lateral and depth variations in seismic structure suggest a complex history. Studies of azimuthal anisotropy have shown the presence of laterally varying layering within the cratonic lithosphere (e.g. Levin et al. 1999, Deschamps et al. 2008, Yuan and Romanowicz 2010), which may indicate different modes and/or times of formation of the top c.a. 100 km of this lithosphere. This is also suggested by fine scale studies of converted and reflected phases, which indicate the presence of a sharp mid-lithospheric discontinuity (MLD) within the craton, marking the top of a mid-lithospheric low velocity zone (Thybo and Perchuc 1997, Bostock 1998, Abt et al. 2010, Fischer et al. 2010, Rader et al. 2015, Ford et al. 2016) and even possibly several mid-lithospheric discontinuities (Calò et al. 2016). In addition, there is evidence from shear wave radially anisotropic tomography for separation between blocks of different crustal ages extending to depths of at least 150 km (e.g. Yuan et al. 2014).

Much of this finer scale structure has been highlighted owing to the availability of data from the dense broadband USArray TA deployment. With the

completion of the coverage of the conterminous US, as well as availability of data from Canada and Greenland, it is now possible to further refine shear wave tomographic images of North America, and in particular of the stable Proterozoic and Archean provinces, to try and improve our understanding of its formation. It is also an unprecedented opportunity to experiment with improved waveform-based tomographic techniques.

In a previous study, we presented a radially anisotropic shear velocity model of the North American upper mantle based on a combination of long period teleseismic and regional waveform data (Yuan et al. 2014) The regional waveform data (down to 40 s period) were, for the first time at this scale, compared to 3D synthetics computed using RegSEM (Cupillard et al. 2012), a Spectral Element Method (SEM) code appropriate for continental scale wavefield computations. Due to the extremely lengthy computations that would have been necessary to compute it numerically at each iteration of the inversion, the predicted teleseismic wavefield was, instead, computed using Non-Linear Assymptotic Coupling Theory (NACT, Li and Romanowicz 1995), a methodology based on normal mode perturbation theory, that is approximate, but computationally more efficient, and has been used in the development of several generations of global and continental scale shear

velocity models (Li and Romanowicz 1996, Mégnin and Romanowicz 2000, Gung et al. 2003, Panning and Romanowicz 2006, Yuan et al. 2011)

The resulting 2014 model of North America presents some interesting features, in particular a correlation of radial anisotropy structure with lithospheric blocks corresponding to different orogenies in the eastern US and continental shelf. While more rigorous than inversions practiced by most groups and based on the path-average surface wave approximation, this mixed methodology nevertheless presents some inconsistencies from the theoretical point of view, since the predicted wavefield through the target model space is computed with different theories for teleseismic and regional distance data.

To better integrate teleseismic data into our regional tomographic inversions, we developed a general framework called "Box Tomography" (see Masson et al. (2013), Masson and Romanowicz, 2016a,b) that allow us to consistently model and invert both teleseismic (i.e. associated with sources or receivers outside of the imaged region) and regional (i.e. associated with sources and receivers within the imaged region) waveform data using accurate numerical methods such as SEM. In Box tomography, prior to the inversion, the seismic wavefield generated by teleseismic sources is first modeled nu-

merically at the global scale for a given reference model and recorded at the surface of the region to be imaged. This reference wavefield is then used to construct virtual sources lying at the boundary of the regional modeling domain and reproducing the original wavefield as illustrated in Figure 3. Once the teleseismic sources have been moved (i.e. replaced by virtual sources) within the regional modeling domain, the tomographic inversion can be performed efficiently in a classic manner (i.e. using regional modeling only) as the teleseismic data are accounted for seamlessly thanks to the virtual sources. Related concepts have been proposed to account for teleseismic data into regional imaging (e.g. Wang et al., 2016 Monteiller et al., 2015), however, in these studies the global modeling of the reference wavefield is performed using a faster method that do not account for the effects induced by the 3D structure of the Earth outside the regional modeling domain. In this paper, we present the first application of Box tomography, where the 3D structure is accounted for outside the imaging box, to continental scale waveform tomography in North America.

## 2 Methodology

Many studies have inverted for continental scale structure, in particular in North America, using fundamental mode and, in some cases, overtone surface wave dispersion data or waveforms observed at teleseismic distances. The usual practice is to first consider the best possible global scale tomographic shear wave velocity model, compute predictions of observables in this model using an approximate theory, generally the surface wave path average approximation (e.g. Nettles and Dziewoński 2008, Bedle and van der Lee 2009, Schaeffer and Lebedev 2014), or, in our group, NACT (Marone et al. 2007, Yuan et al. 2011). In the case when secondary observables such as dispersion data are considered, the contribution from outside of the target region is calculated once and for all in the background global model, and subtracted from the observed dispersion data. The resulting residual is attributed to structure in the target region and the tomographic inversion proceeds within this target model volume. When inverting waveforms, and in particular when a more accurate theory than the PAVA is considered, such a simple procedure is not possible, and it is necessary to recompute the synthetic teleseismic waveforms, at each iteration, in a 3D model which is fixed outside of the target region, and updated only within it. This leads to

substantial computations, even in the case of an approximate theory such as NACT, and becomes prohibitively expensive, if the 3D teleseismic wavefield is computed using SEM or another accurate numerical method, as one aims to include increasingly shorter periods.

To overcome this issue, we take advantage of the "Box Tomography" theory which allows to combine teleseismic and regional waveforms in a consistent manner to image regional targets at arbitrary locations. This general framework accommodates for arbitrary acquisition setups (i.e. with sources and receivers located outside the regional imaging box), is compatible with most popular numerical methods such as SEM or FD, and can produce exact seismograms and sensitivity kernels (i.e. similar to those obtained when solving the problem globally). In this study, we limit ourselves to the situation where both regional and teleseismic events are employed but where all the seismic stations lie within the regional computational domain. Furthermore, we neglect some higher order scattering effects as proposed by Masson and Romanowicz (2016a). In this situation, Box Tomography is particularly efficient as the computational effort to account for teleseismic data in regional inversions is limited to a few global scale simulations that are done once and for all prior to the inversion. Masson and Romanowicz (2016b) showed

that this approach can produce accurate regional tomographic images even though the elastic structure outside the imaged region is neither fully known prior to the inversion nor updated during the inversion.

Here, we apply this methodology to the case of teleseismic three component waveform data observed at stations within North America, combined with "regional" waveform data for which both earthquakes and stations are located within the target region. This is the first time this methodology is applied in practice, and this study represents a proof of concept for this approach. Adding teleseismic data allows better azimuthal coverage of the target region than can be achieved using only the regional dataset and eventually provides for the inclusion of constraints from additional phases such as, for example, teleseismic SS phases reflected inside the target region.

## 2.1 Dataset and model parametrization

The dataset includes three component acceleration waveforms from 2860 permanent and temporary broadband stations located in the target region, a  $89^\circ \times 89^\circ$  area encompassing most of north America (Figure 1). We considered two different datasets:

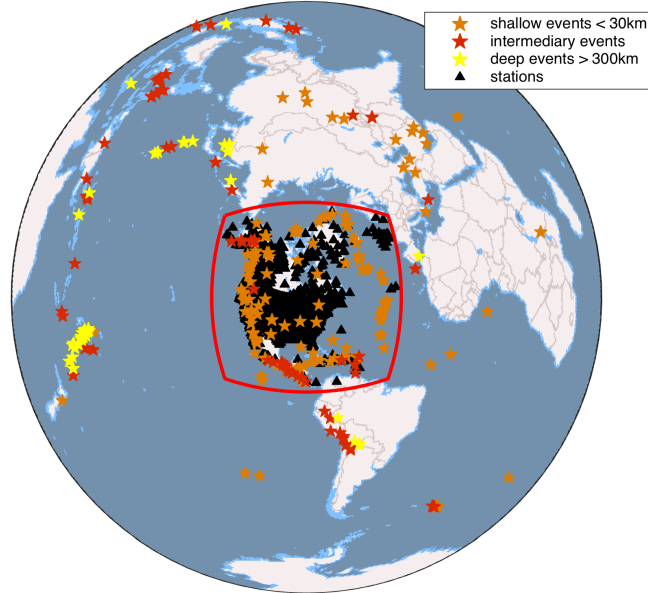


Figure 1: Source and station distribution for the new North American inversion. Black triangles show the seismic stations. Stars are 155 regional events, in addition to 122 teleseismic events. Orange stars indicate events shallower than  $30\text{km}$  deep, Yellow stars for deeper than  $300\text{km}$  and red one are in between. Thick red line indicates the boundaries used for the RegSEM forward simulation, which extends 89 by 89 horizontally and down to 1600 km and contains all stations and regional events.

- a regional dataset consisting of 155 events ( $4.5 < M_w < 6.0$ ) for which sources are located within the target region.
- a teleseismic dataset, consisting of 122 events ( $5.5 < M_w < 6.9$ ) for which sources are located outside of the target region.

The waveforms are filtered between 40 and 400 s, with corner frequencies

of 53 and 250 s, and windowed into wavepackets, according to the procedure of Li and Romanowicz (1996) allowing different weights to be applied according to relative amplitude of individual wavepackets, redundancy of paths and signal to noise ratio. This weighting step is crucial, as it homogenizes the data coverage within the region and provides a way to construct the data covariance matrix  $C_D$ , which we approximate as a diagonal matrix. At each iteration of the inversion, only those wavepackets are considered that satisfy predefined goodness of fit criteria compared to synthetics calculated in the current 3D model, which avoids cycle slipping in our time domain waveform inversion procedure. As the model improves, at each iteration, additional wavepackets are included. The total number of wavepackets of fundamental and overtone Love and Rayleigh waves is given in Table 1, and provides a good azimuthal coverage within the NA continent (Figure 2).

In addition to long period waveforms, we also consider a group velocity dispersion dataset (Shapiro and Ritzwoller 2002) provided in the form of  $1^\circ \times 1^\circ$  maps between 25 and 100 s. The shorter periods (below 60 s) are used to constrain our homogenized crustal structure at each iteration, as described below, while the entire period range is included during the inversion for mantle structure, providing additional constraints for structure in the

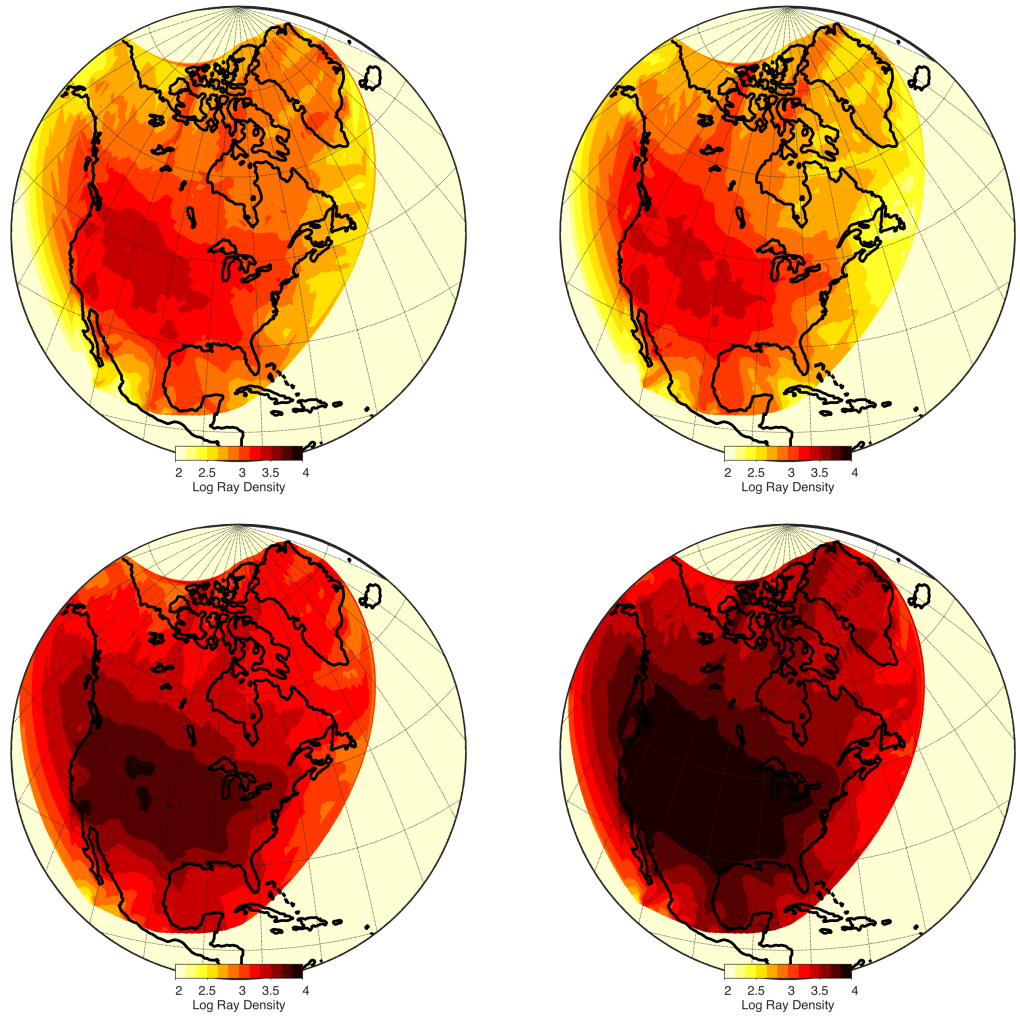


Figure 2: Density coverage for each component and all gathered.

shallow parts of the mantle that are consistent with the treatment of the crust.

As in our previous work at the global scale (French et al. 2013, French and Romanowicz 2014), we do not rely on an existing layered crustal model. There are several drawbacks to considering such models. First, they are constructed using data for limited regions that are then extrapolated to other regions based on a tectonic regionalization, and may not always fit real waveform data very well. Second, the inclusion of thin low velocity layers slows down the SEM computation significantly. Instead, we compute a radially anisotropic smooth crustal model on a  $2^\circ \times 2^\circ$  grid through Monte Carlo Markov Chain (MCMC) simulation constrained by the group velocity dispersion data. This process is a sort of "homogenization" (e.g. Backus, 1961; Capdeville and Marigo, 2008), which yields a crustal model equivalent to a real crust within the period range of the data used to constrain it (i.e. for periods longer than 20s). The thickness of the crust is a priori chosen as that of model Crust2.0 (Bassin et al. 2000) where it is larger or equal to 30 km, and it is fixed at 30 km otherwise. This results in a smooth, but realistic crust within most of the continent, and a crustal model that is not interpretable in the border regions of our model space (i.e. in the oceans and

borders of the continent). We have shown that this does not bias the mantle structure obtained below 50 km (French and Romanowicz 2014). At each iteration of the inversion, we only invert for structure below 30 km depth, and subsequently recompute the crustal model for the next iteration by applying our MCMC approach with mantle structure fixed to be that of the current iteration model. The procedure is described and discussed in detail in French and Romanowicz (2014)

Assuming that our azimuthal coverage is everywhere sufficient within our target region (Figure 2), we here solve only for radially anisotropic structure and specifically for two of the 5 parameters that describe such a structure, the two parameters to which long period surface waveforms are the most sensitive: isotropic velocity  $V_S$  and the anisotropic parameter  $\xi = \frac{V_{SH}}{V_{SV}}^2$ , where  $V_{SH}$  is the velocity of waves polarized horizontally and  $V_{SV}$  that of waves polarized vertically . The other three parameters and density are constrained through empirical scaling relationships, following Montagner and Anderson (1989), and are based on laboratory measurements for upper mantle rocks. If (A,C,F,L and N) are the 5 elastic parameters describing a radially anisotropic (or VTI) medium (Love, 1927), then:

$$N = \rho V_{SH}^2, \quad L = \rho V_{SV}^2, \quad A = \rho V_{PH}^2, \quad C = \rho V_{PV}^2 \quad (1)$$

then the medium can equivalently be described by the 5 parameters  $(V_S, V_P, \xi, \phi, \varepsilon)$  where:

$$V_S = \sqrt{\frac{2V_{SV}^2 + V_{SH}^2}{3}} V_P = \sqrt{\frac{V_{PV}^2 + 4V_{PH}^2}{5}} \xi = \frac{N}{L}, \quad \varphi = \frac{C}{A}, \quad \eta = \frac{F}{A - 2L} \quad (2)$$

The scaling parameters considered are (Montagner and Anderson 1989)

$$\frac{\delta(V_P)}{\delta(V_S)} = 0.5, \quad \frac{\delta(\rho)}{\delta(V_S)} = 0.33, \quad \frac{\delta(\eta)}{\delta(\xi)} = -2.5, \quad \frac{\delta(\varphi)}{\delta(\xi)} = -1.5, \quad (3)$$

We prefer parametrization in terms of  $V_S$  and  $\xi$ , rather than  $V_{SH}$  and  $V_{SV}$ , as this allows us to consider different spatial resolution and apply higher damping in the inversion to the less well resolved anisotropic parameter  $\xi$ , rather than having to reconstruct this parameter from differences in perturbations in the two quantities  $V_{SH}$  and  $V_{SV}$ , which would limit the resolution allowed in isotropic velocity.

In previous studies (Marone and Romanowicz 2007, Yuan and Romanowicz 2010), after inverting for radial anisotropic structure (Marone et al. 2007,

Yuan et al. 2011), we also inverted for azimuthal anisotropy, by adding constraints from SKS splitting measurements. This step will be the topic of a separate publication.

The target model space is geographically defined as shown in Figure 1, and is limited in depth down to 800 km. As in our previous tomographic studies, the model space is parametrized in terms of 26 cubic splines  $\nu(r)_q$  vertically (Mégnin and Romanowicz 2000) from the core-mantle boundary to the Moho, although we invert for structure only in the top 16 splines, corresponding to the top 700-800 km of the mantle. The spline nodes are spaced more closely at shallow depths, and located at the following radii: 5690, 5810, 5910, 5900, 6061, 6101, 6131, 6161, 6191, 6221, 6241, 6261, 6281, 6301, 6321, 6341 km. Laterally, we parametrize our model in terms of spherical splines  $\beta(\theta, \phi)_p$  (Wang and Dahlen 1995). The combination of vertical and spherical splines constitutes a local basis for the description of smooth functions within the model volume. Thus, the value of a model parameter  $m(r, \theta, \phi)$  can be computed at any point in space given the set of spline coefficients  $m_{pq}$ :

$$m(\theta, \varphi, r) = \sum_p \sum_q m_{pq} \beta_p(\theta, \varphi) \nu_q(r) \quad (4)$$

The spherical spline parametrization has the advantage of allowing for variable grid parametrization, which can be adjusted according to data coverage (e.g. Marone et al. 2007). In our case, outside of the target region, we adopt a "level 6" spherical grid for  $V_S$  ( $2^\circ$  knot spacing) and a "level 4" spherical grid for  $\xi$  ( $8^\circ$  knot spacing), consistent with the parametrization of SEMUCB\_wm1. Inside the well-sampled target region, we define a level 7 spherical grid ( $1^\circ$  knot spacing) for  $V_S$  and level 6 ( $2^\circ$  knot spacing) for  $\xi$ .

## 2.2 Forward modelling

During the inversion, all the synthetic seismograms are computed using the regional SEM code RegSEM (Cupillard et al. 2012) that takes into account effects of oceans, topography/bathymetry, ellipticity, and anelasticity, and where the computational domain is truncated using absorbing boundaries. The synthetic seismograms associated with regional data (i.e. where both the seismic stations and the earthquake are located within the regional modeling domain) do not require any specific treatment and are modeled as in our previous studies (e.g. Yuan et al. 2014). The synthetic seismograms associated with teleseismic data (i.e. where the earthquake and the seismic stations are located outside and inside the regional modeling domain, respectively) are

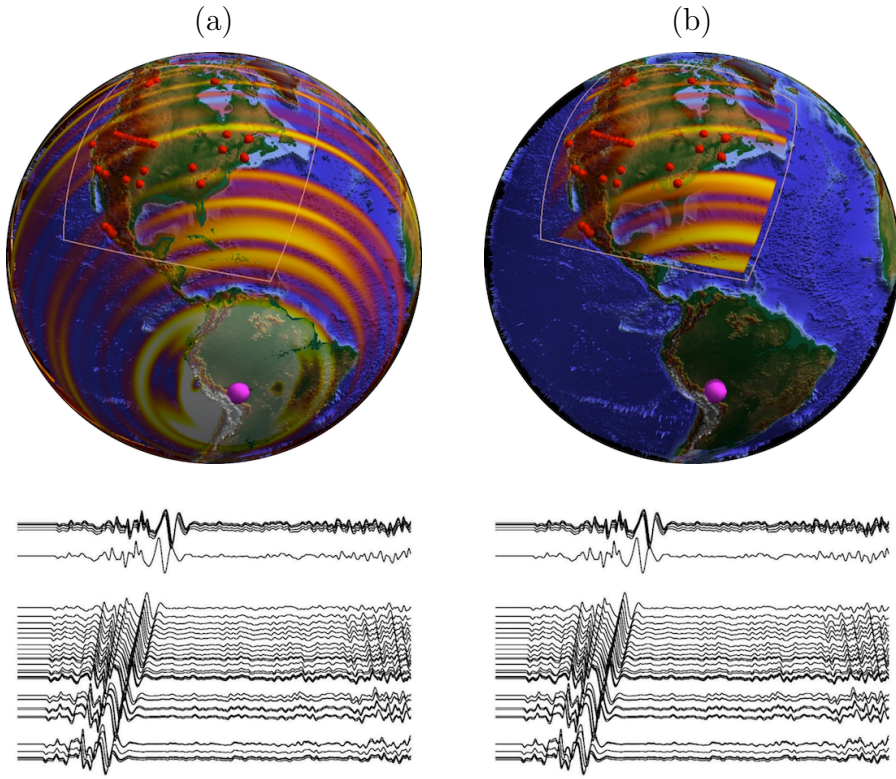


Figure 3: Comparison between a global scale simulation and a regional scale simulation of wave propagation following an earthquake in south America. The seismograms corresponds to the recordings at 37 station located in north America (red spheres). The pink sphere shows the epicenter of the earthquake. In (a), the wavefield is modeled globally using the spectral element method Specfem3D\_globe (Komatitsch 2002). In (b), the wavefield is modeled regionally using the RegSEM. During the inversion, all the synthetic seismograms are computed using the regional SEM code RegSEM (Cupillard et al. 2012) code and regenerated thanks to virtual sources located around the computational domain (see Masson et al. 2013). The sismograms in (b) are exactly similar to those in (a), however, the computational effort is greatly reduced in the regional simulation (b).

obtained using a two step procedure as proposed by Masson and Romanowicz (2016). Prior to the inversion, the wavefields generated by teleseismic earthquakes are computed globally within our starting model (*SEMucb\_wm1*) and using an adapted version of SPECFEM3D\_globe (Komatitsch 2002). During these global simulations, the 3 component displacement wavefield is recorded at a set of points with locations prescribed by the RegSEM code. Within the regional solver RegSEM, these points are the coallocation or Gauss-Lobatto-Legendre (GLL) points belonging to the one element thick surface surrounding the regional modeling domain (see Masson et al. 2013). Notice that our procedure do not require to store the stress nor the strain wavefield which are computed naturally by the regional solver, this makes it easy to swap between different codes for modeling global wave propagation (i.e. any code that outputs displacement seismograms can be used as such). Because the Courant criteria which ensure the stability in SEM often leads to oversampling, we compress the recordings versus time using a least square B-spline transform (Unser et al., 1993ab), we found this approach more efficient and practical than the more classic decimation/interpolation scheme. We typically achieve data compression ratio lying between 10 and 100 with no significant loss of accuracy. During the inversion, the global recordings are transformed to vir-

tual sources that regenerate the global wavefield regionally, this operation is done on the fly by the RegSEM code and illustrated in Figure 3b.

Overall, the additional computational effort to account for teleseismic event consists of one global simulation per teleseismic event that are done once and for all before the inversion starts.

### 2.3 Inverse modelling

In continuity of our previous work (e.g Marone et al. 2007, Yuan et al. 2011, Yuan and Simons 2014), we use a hybrid iterative inversion scheme where, at each iteration, the forward wavefield is computed accurately using SEM, but the inverse step is solved using the formalism of Tarantola and Valette (1982) with sensitivity kernels calculated approximately using normal mode perturbation theory. This allows us to apply a fast converging Gauss-Newton quadratic optimization scheme. As shown in Tarantola (2005), and in Appendix A of Lekić and Romanowicz (2011), it is far more important to use an accurate forward modelling scheme to compute the misfit function, while inaccuracies in the theoretical treatment of kernels result in smoothing errors that can be compensated for in subsequent iterations. Currently popular "adjoint tomographic" approaches (Zhu et al. 2015, Bozdağ et al. 2016) do

compute the numerically exact gradient, however, they also need to apply smoothing operators and regularization, which degrades the accuracy of their kernels. Importantly, they rely on a linear optimization scheme (conjugate gradient method), which is characterized by very slow convergence.

Our misfit function is defined in the time domain from the point by point differences between observed and synthetic waveforms by:

$$2\Phi(m_k) = [d - g(m_k)]^T C_d^{-1} [d - g(m_k)] + [m_p - m_k]^T C_m^{-1} [m_p - m_k] \quad (5)$$

where  $m_k$  represents the model estimate at the k-th iteration,  $d$  is the data vector (waveform discretized in time or group velocity as a function of period) and  $g(m_k)$  is the corresponding discretized wavefield computed using SEM, or the predicted group velocity dispersion.  $m_p$  is the model prior (i.e. the 3D starting model) and  $C_m$  and  $C_d$  represent a priori model and data covariance matrices, respectively. Minimizing  $\Phi$  in the sense of the L2 norm leads to the equation for the k+1 model update:

$$m_{k+1} = m_k + (C_m G_k^T C_d^{-1} G_k + I)^{-1} (C_m G_k^T C^{-1} [d - g(m_k)] + m_p - m_k) \quad (6)$$

where  $G$  is the matrix of Frechet derivatives of  $g(m)$  calculated at  $m_k$ . We

compute  $G$  using NACT or the Path Average Approximation (PAVA, Woodhouse and Dziewonski (1984)), depending on the distance range of the corresponding source-station path. NACT and PAVA are both asymptotic (high frequency) approximations to normal mode perturbation theory. The PAVA includes along branch mode coupling only and is the standard surface wave approximation (e.g Mochizuki 1986, Romanowicz 1987), as used for example in Woodhouse and Dziewonski (1984), in which a frequency shift and distance shift are introduced for each mode to account for the effects of heterogeneous structure. The corresponding kernels are "1D", i.e. they only depend on the average structure between the source and the receiver. This approximation is valid for single-mode seismograms, such as fundamental mode surface waves (e.g Romanowicz et al. 2008). NACT includes across branch-coupling, in addition to PAVA, which brings out 2D sensitivity of waveforms in the vertical plane containing the source and the receiver. NACT breaks down when the distance between the source and station is short, so we compute kernels using NACT for epicentral distances larger than  $15^\circ$ , and PAVA for shorter distances. Neither PAVA nor NACT consider off-great circle plane sensitivity (i.e. focusing effects, e.g. Zhou et al. (2005)). These effects become important for accurate amplitude fitting. With our choice of misfit function,

we are first and foremost fitting the phase, and for that, the 2D effects in the vertical plane are dominant, and important especially for overtones, as illustrated in Romanowicz et al. (2008).

## 3 Results

The tomographic inversion results for  $V_S$  and  $\xi$  are presented in figures (to be defined). We divide the model description and interpretation into two parts, focusing first on the continent-wide structure and then, in more detail, on different regions.

### 3.1 Continental model

As observed in many other studies, average profiles of  $V_S$  within North America (NA) in the shallow upper mantle is higher compared to Global average profiles biased by ocean structures as shown in Figure 5. The difference is clearly distinct until ca. 270km and then fade away deeper, though, NA remains slightly higher than the global average. The global negative gradient of  $V_S$  near 150km is here less pronounced beneath the continent by the influence of the positive gradient beneath the cratonic part. NA average of

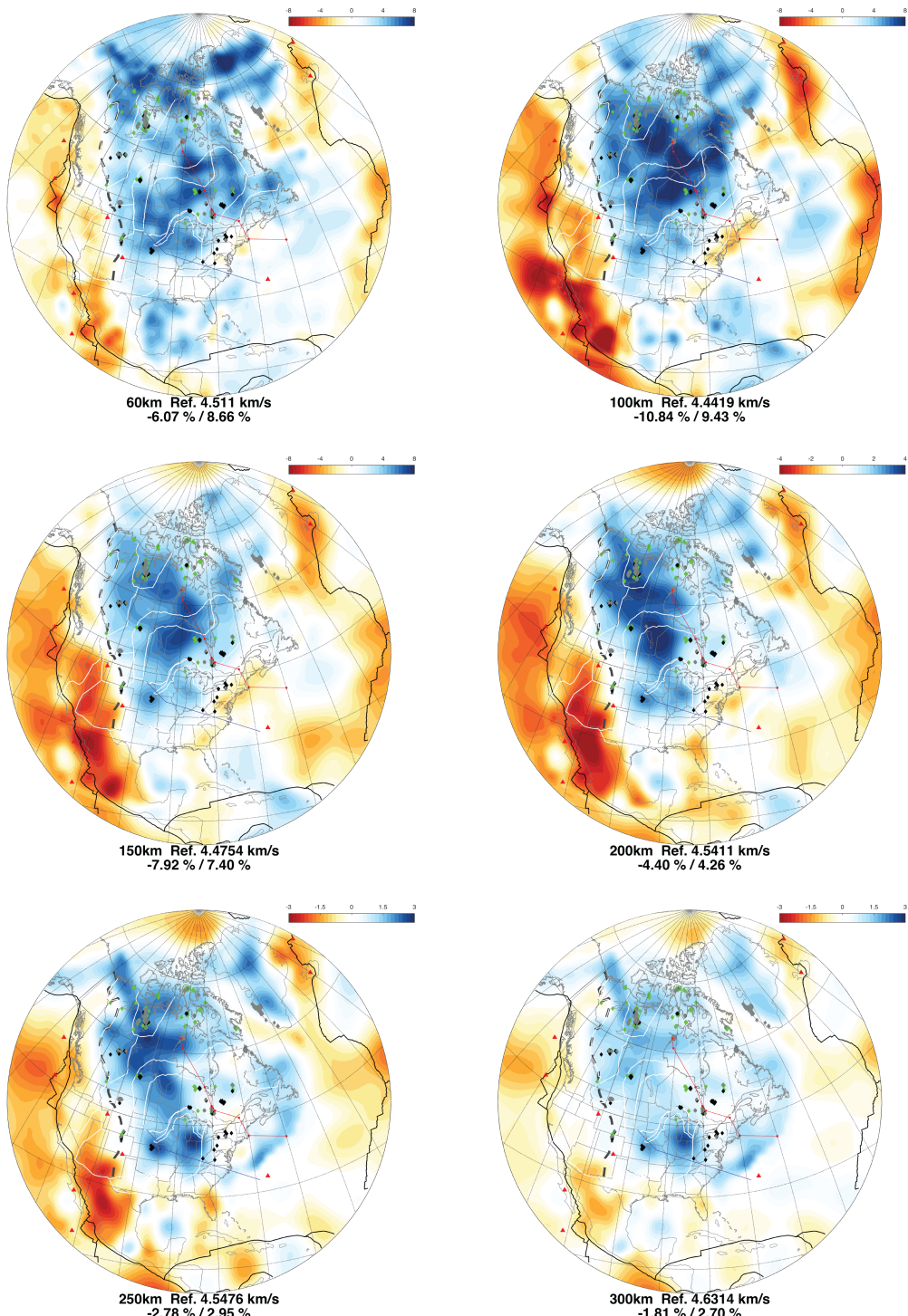


Figure 4: 3D isotropic shear wave velocity structure of the continent. Map views are shown from 60 km down to 300 km, shown as variations with respect to the global mean (thick black line in Figure 5). <sup>24</sup>

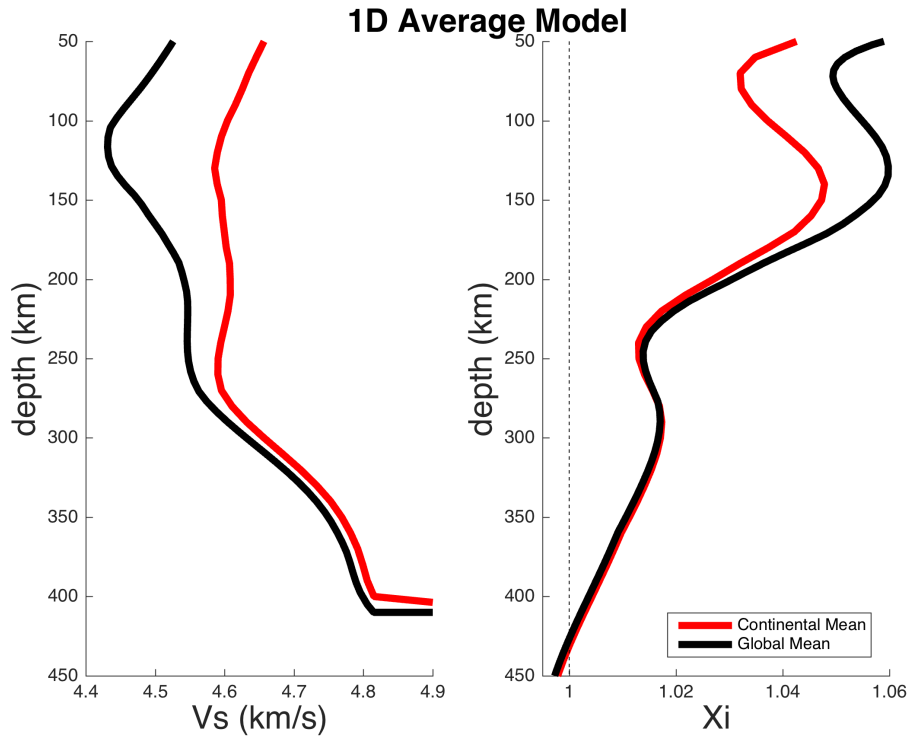


Figure 5: 1D profiles of the global mean and the continental mean

$\xi$  is lower than the global average, the latter influenced by the strong  $\xi > 1$  oceanic signature where shearing is more important. Both trends are similar, while maxima and minima are always slightly deeper than globally and the change from  $V_{SH} > V_{SV}$  to  $V_{SH} < V_{SV}$  is reached at ca. 420km.

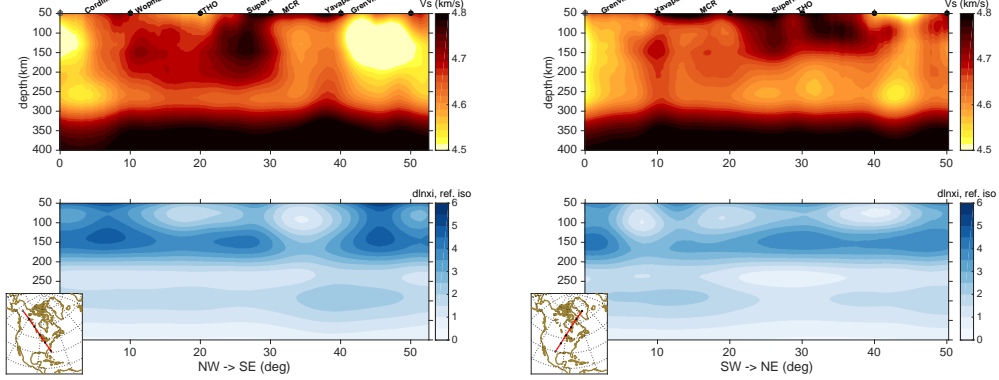


Figure 6: Cross Section of the lithospheric core

### 3.2 Beneath the craton

Our study confirms the presence of a thick cratonic root with faster than average  $V_S$  down to 250km deep, with highest velocities, ca.  $4.8 \text{ km.s}^{-1}$ , located at depths shallower than at most 150km. Laterally, the cratonic root in terms of  $V_S$ , coincides with precambrian aged crust. The western and eastern/south eastern edges follow the Rocky Mountain Front (RMF) and the Llano-Grenville Front respectively. The northern part is delimited by the coastline of the Arctic ocean including the arctic archipelago and Greenland. These lateral edges are well observed until 150km, below, the cratonic root retracts toward the center of the archaeal continent beneath Slave, Hearne/Rae and western Superior cratons. Everywhere within the lithosphere, a negative gradient of  $V_S$  is observed with a minimum of ca.

$4.6 \text{ km.s}^{-1}$  reached at  $300 \text{ km}$ . Deeper, this gradient switches to a positive trend. While the beginning of the negative gradient shows a topography, the bottom of the gradient located beneath Slave, Hearne/Rae and western Superior cratons; appears very flat.

As observed in Gung et al. (2003); down to  $250 \text{ km}$  low positive ( $< 2\%$ ) anomalies of  $dln(\xi)$  (Compared to an isotropic  $\xi$ ) are observed in the whole craton. In contrast with the oceanic surrounding that shows strong positive anomalies ( $> 4\%$ ). The gulf of Mexico and the southern part of Greenland show  $\xi$  anomalies that are comparable to oceanic signature. The Grenville and Appalachian shelf (including the eastern Superior craton) show also higher  $\xi$  anomalies comparable to oceanic signature. Deeper, positive anomalies are emerging beneath archaean Slave/Rae blocks/Eastern Superior and proterozoic North THO/Yavapai/Mazatzal/Great Rhyolites provinces, following highest velocities anomailies. However  $dln\xi$  anomalies remain low beaneath the archaean eastern Superior block. In the whole lithosphere,  $\xi$  is higher than 1 which means that  $V_{SH} > V_{SV}$ .

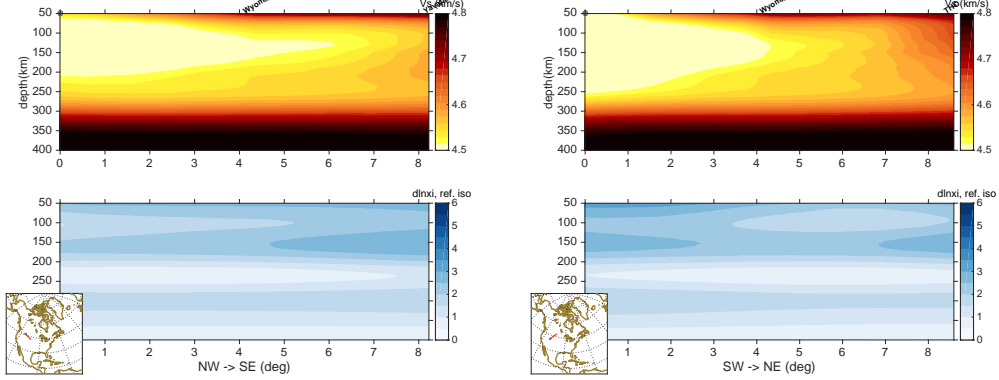


Figure 7: Cross Section of the Wyoming lithosphere

### 3.2.1 Wyoming

The Archaean aged Wyoming craton does not show as high anomalies as within the craton nucleus as shown in figure 7. It is split into 2 distinctive part. A western part showing low velocities influenced by the active tectonic with a radially positive gradient. In contrast with the eastern part showing higher velocities with a radially negative then positive gradient. The depth of negative gradient's minima is variable, from 70 (western part) to 250km (eastern part) deep. The separation between the two areas coincides with the RMF.

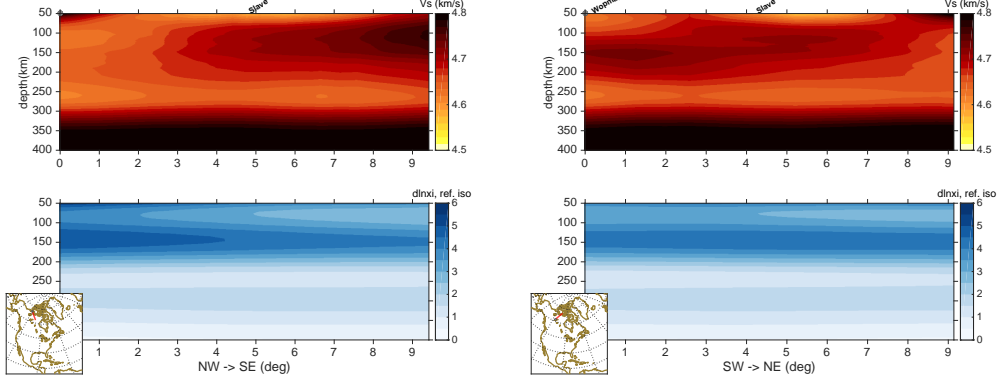


Figure 8: Cross Section of the Slave lithosphere

### 3.2.2 Slave

The Archaean aged Slave craton shows typical lithospheric craton signatures with higher than average velocities as shown in figure 8. It shows in the entire region a positive velocity gradient with a maximum of ca.  $4.8 \text{ km.s}^{-1}$  associated with a maximum of  $\xi$  at ca.  $150 \text{ km}$  deep. Deeper, a negative gradient is observed with a minimum of ca.  $4.6 \text{ km.s}^{-1}$  at ca.  $250 \text{ km}$  deep. The topography of the extrema appears flat. (Est ce que c'est une caractéristique d'un craton stable non déformé?) Although the Slave lithosphere shows highest velocities at  $150 \text{ km}$ , above  $100 \text{ km}$  velocities are slightly higher than the continental average ( $d\ln(V_S) < 4\%$ ).

### 3.2.3 Superior Craton

In our model, the Superior craton can be split in two parts: The western part showing typical cratonic structures while the eastern part shows slower velocities at all depths. Below 150km, velocity anomalies are below 2% (almost 0%).

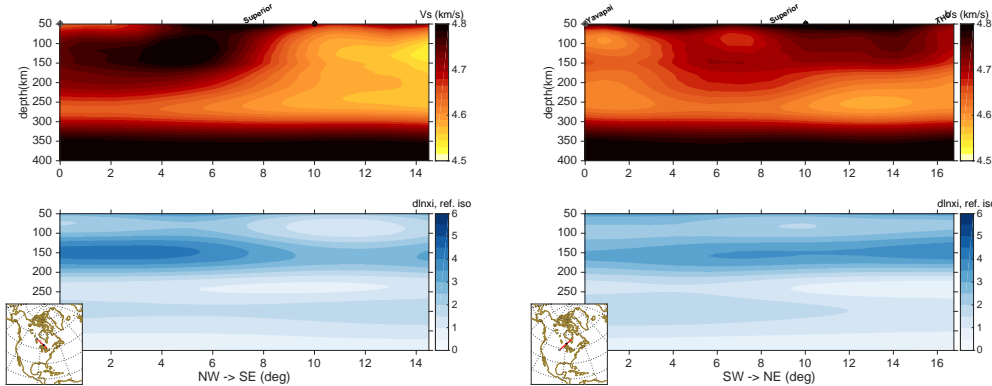


Figure 9: Cross Section of the western Superior lithosphere

**Western part** The Archaean aged Superior craton shows typical lithospheric craton signatures with higher than average velocities as shown in figure 9. It shows in the entire region a positive velocity gradient with a maximum of ca.  $4.8 \text{ km.s}^{-1}$  associated with a maximum of  $\xi$  at ca. 150km deep.

Deeper a negative gradient is observed with a minimum of ca.  $4.6 \text{ km.s}^{-1}$  at ca. 250km deep. Opposed to the Slave craton, the topography of the

extrema is variable. From SW to NE, the core of maximum velocity can reach between 70 and 150km of thickness. Beneath the maximum velocity region of ca. 150km the negative gradient appears steeper than beneath the 70km one, while the topography of the deeper positive gradient appears flat. At the south-eastern part of the western Superior, close to the Mid-Lithospheric rift, we can observe the thinning of the cratonic lithosphere when crossing the Grenville front. The band of minimum velocity within the cratonic root has similar amplitudes, in terms of velocity, than beneath the younger lithosphere but at shallower depths between 100 and 150km. Following the Great Meteor track built by Heaman and Kjarsgaard (2000), which crosses the Superior craton, it is interesting to note that the low velocity channel beneath the base of the lithosphere shows lower velocities than usually observed beneath the other Archaean cratons. This slow anomaly corresponds to the V-shape dent, or divot, observed by van der Lee and Nolet (1997) who explained the feature by the presence of water in the mantle. We observe at 250km that the slow anomaly goes further inland and crosses the Superior Craton northward until the Hudson bay following the GMT.

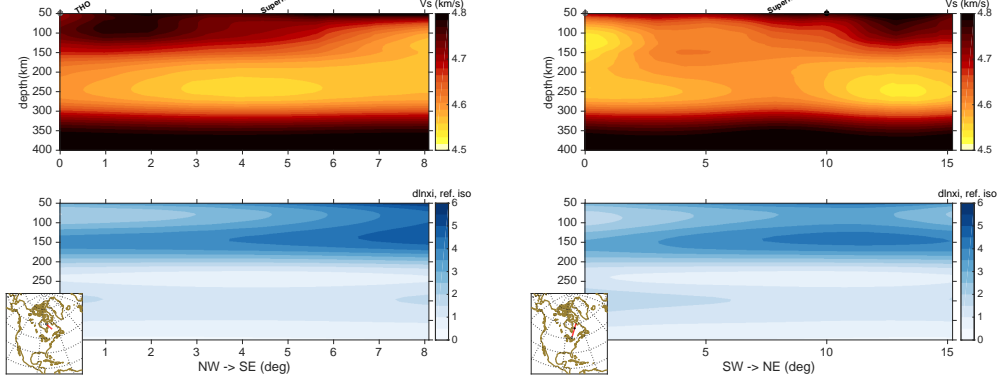


Figure 10: Cross Section of the western Superior lithosphere

**Eastern part** Compared to its western part, the structure here shows differences as shown in figure 10. . Fast velocities are present down to 150km deep but are slower. The negative gradient is steeper and the minimum is radially thicker. However at the center, the minimum channel is not continuous and shows higher (still slower than the center of the western Superior) velocities.

### 3.2.4 Trans Hudson Orogen

The Trans Hudson Orogen (THO) is a belt of Paleo-Proterozoic aged region. It refers to a major tectonic event (between 2.0 to 1.8Ga) that welded Archaean blocks to form the Laurentia Craton. It is interesting to notice that at shallower depths than 100km, the proterozoic THO (including the Sask craton) which welded the Superior and Rae/Hearne cratons, shows lighter

(i.e, +4% compared to +8%) positive anomalies than its archaean surrounding. While most of the proterozoic root start to thin out at 150km, the THO at the vicinity of the hudson bay shows as high anomalies as Rae/Hearne and Superior areas.

### 3.2.5 Yavapai Mazatsal region

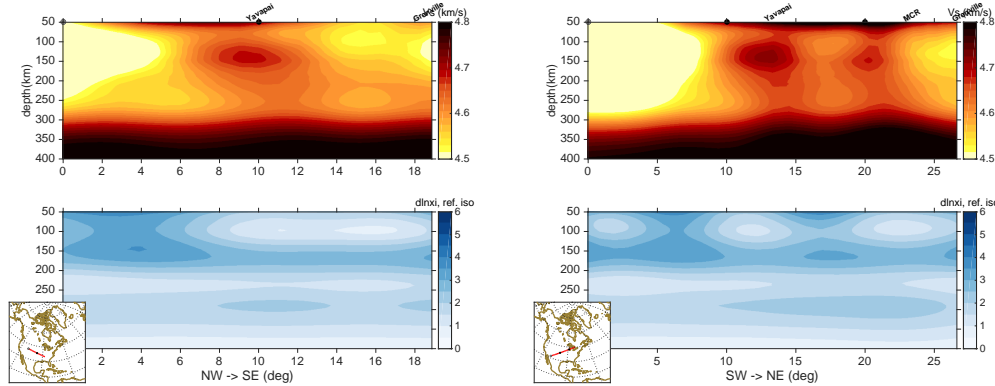


Figure 11: Cross Section of the Yavapai and Mazatzal lithosphere

Yavapai-Mazatzal orogens from 1.8 to 1.6 Ga represent zones of accretion for Proterozoic material and mark the amalgamation of the archean cores. (Hoffman 1988)

Cross section of the region are represented in figure 11. West to the RMF, the region shows low velocities influenced by the active tectonic with a radially positive gradient. The north eastern part shows velocity anomalies slightly lower than the Archaean nucleus. Velocity maxima of  $4.8\text{km}\cdot\text{s}^{-1}$

are located shallower than  $100\text{km}$ . Below, the radially negative gradient is observed and shows the same characteristic than the eastern Superior craton. It is interesting to note that, beneath Nebraska and Kansas, a high velocity anomaly of about  $4.7\text{km}\cdot\text{s}^{-1}$  is present until ca.  $170\text{km}$  (while it is  $120\text{km}$  in most of the region) where cretaceous aged kimberlites are sampled. These kimberlites indicate a lithosphere thickness of about  $160\text{km}$  and have been affected by asthenospheric upwelling related to the Mid-Continent Rift System. (Griffin et al. 2004)

### 3.3 Surrounding oceanic

Our inversion is focusing on the continental part, as shown in our spatial parameterization (i.e. see figure...) where the region is sampled by data. Except the oceanic borders of NA, further away, the structure has not been updated from SEMucb\_wm1 (French and Romanowicz 2014).

#### 3.3.1 Eastern Passive margin

As in Schaeffer and Lebedev (2014), Yuan et al. (2014), James et al. (2014), Silveira and Stutzmann (2002), Mocquet and Romanowicz (1990), we observe along the negative anomaly structure following the Appalachian continental

shelf, a stretched positive anomaly structure from the Suwanne terrane in Florida to the Avalonian terranes of New-Scotland. At  $60\text{km}$  it is made of several blocks of at most +3% anomalies embedded in a +2% structure. At  $150\text{km}$ , the structure is split into 2 blocks by a slow anomaly comprising both the Great Meteor (GMT) and Bermuda tracks, and further southeast, the Low Velocities Fingers (LVF) observed in French et al. (2013).

Such structure would correspond to late proterozoic gondwanian continental terranes that formed during the Pan African orogenesis (Kennedy 1964) and remained attached to the North American margin during the opening of the Atlantic ocean. (e.g. Thomas 2006) On the continental shelf, authors (e.g. O'Brien et al. 1983, Nance et al. 2002) identified the west Avalonian terranes of pan-african affinity as in Florida (see Smith 1982) that might have been underlaid by a thin (ca.  $100\text{km}$ ) lithosphere before the Pangaea assembling. (McKenzie et al. 2015)

Fast anomalies are observed beneath the whole gulf of Mexico down to  $150\text{km}$  deep. Despite the proximity with pan-african lithosphere, such high velocity anomalies represent older than  $ca.150\text{Ma}$  oceanic lithosphere. (Müller et al. 2008, Pindell and Kennan 2009) – No Magnetic anomalies recorded as in Pan African, Oceanic seafloor according to Pindel –

### 3.3.2 The Great Meteor track

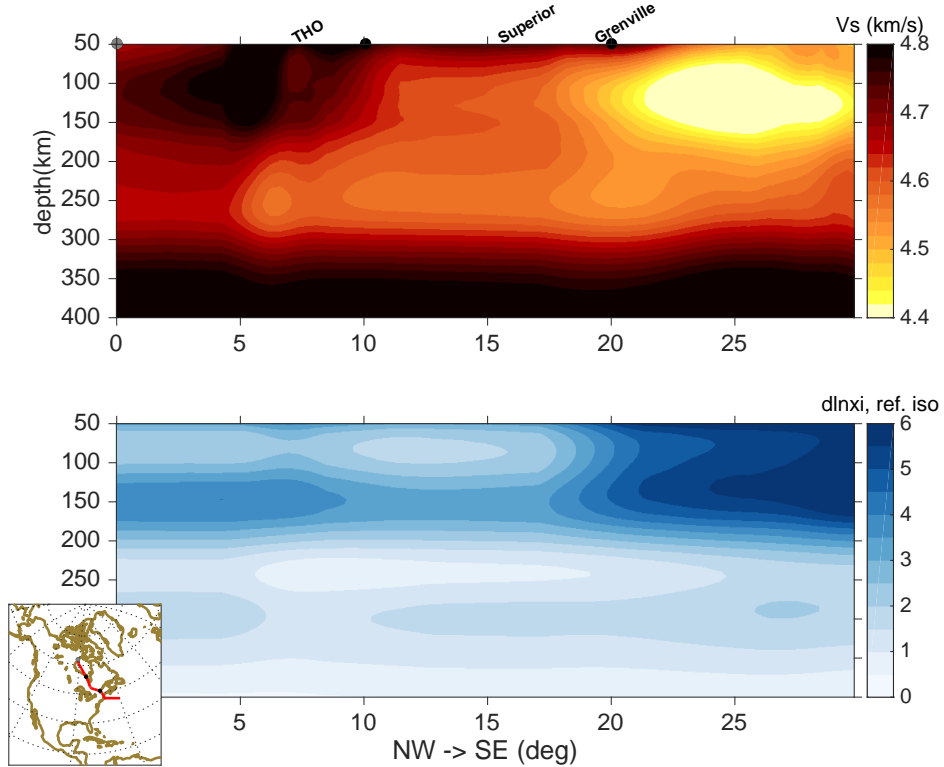


Figure 12: Cross Section of the lithosphere along the Great Meteor track

based on Heaman and Kjarsgaard (2000) construction

Our model images a slow velocity anomaly in agreement with the reconstruction of the Great Meteor Track (thin red line in figure 4) proposed by Heaman and Kjarsgaard (2000). Below 100km the pan african lithosphere is cut in two by a slow velocity anomaly beneath the New England

seamounts (youngest part of the GMT). Further East, the slow anomaly follows the GMT crossing the continental shelf, Appalachian and Grenville orogens down to 200km. This slow anomaly corresponds to the V-shape dent, or divot, observed by van der Lee and Nolet (1997) who explained the feature by the presence of water in the mantle. We observe at 250km that the slow anomaly goes further inland and crosses the Superior Craton northward until the Hudson bay following the GMT. See the cross section along the re-built GMT in figure 12.

Heaman and Kjarsgaard (2000), based on  $U - Pb$  perovskite age determinations of kimberlites, proposed a progressive southeastward younging of kimberlite magmatism throughout much of eastern North America. Considering it as a strong support for small volume mantle melting that have occurred along the continental portion of the Mesozoic Great Meteor mantle plume hotspot track initiated during the opening of the North Atlantic Ocean at about 200Ma. (See figure 4. in Heaman and Kjarsgaard 2000)

Davies (1994) described a process of thermo-mechanical erosion which involves heating-softening of the lithospheric base by a plume tail, followed by mechanical removal of the material due to convective transfer. (Rondenay et al. 2000)

## References

- Abt, D. L., Fischer, K. M., French, S. W., Ford, H. A., Yuan, H., and Romanowicz, B. (2010). North american lithospheric discontinuity structure imaged by PsandSpreceiver functions. *Journal of Geophysical Research*, 115(B9).
- Bassin, C., Laske, G., and Masters, G. (2000). The current limits of resolution for surface wave tomography in north america. *EOS Trans AGU*.
- Bedle, H. and van der Lee, S. (2009). Svelocity variations beneath North America. *Journal of Geophysical Research*, 114(B7).
- Bostock, M. (1998). Mantle stratigraphy and evolution of the slave province. *Journal of Geophysical Research: Solid Earth*, 103(B9):21183–21200.
- Bozdağ, E., Peter, D., Lefebvre, M., Komatitsch, D., Tromp, J., Hill, J., Podhorszki, N., and Pugmire, D. (2016). Global adjoint tomography: First-generation model. *Geophysical Journal International*, page ggw356.
- Calò, M., Bodin, T., and Romanowicz, B. (2016). Layered structure in the upper mantle across North America from joint inversion of long and short period seismic data. *Earth and Planetary Science Letters*, 449:164–175.

Cleary, J. and Hales, A. L. (1966). An analysis of the travel times of p waves to north american stations, in the distance range 32 to 100. *Bulletin of the Seismological Society of America*, 56(2):467–489.

Cupillard, P., Delavaud, E., Burgos, G., Festa, G., Vilotte, J.-P., Capdeville, Y., and Montagner, J.-P. (2012). RegSEM: a versatile code based on the spectral element method to compute seismic wave propagation at the regional scale. *Geophysical Journal International*, 188(3):1203–1220.

Davies, G. F. (1994). Thermomechanical erosion of the lithosphere by mantle plumes. *Journal of Geophysical Research: Solid Earth*, 99(B8):15709–15722.

Debayle, E. and Ricard, Y. (2012). A global shear velocity model of the upper mantle from fundamental and higher Rayleigh mode measurements. *Journal of Geophysical Research: Solid Earth*, 117(B10).

Deschamps, F., Lebedev, S., Meier, T., and Trampert, J. (2008). Stratified seismic anisotropy reveals past and present deformation beneath the east-central United States. *Earth and Planetary Science Letters*, 274(3-4):489–498.

Fischer, K. M., Ford, H. A., Abt, D. L., and Rychert, C. A. (2010).

The lithosphere–asthenosphere boundary. *Annu. Rev. Earth Planet. Sci.*, 38(1):551–575.

Ford, H. A., Long, M. D., and Wirth, E. A. (2016). Midlithospheric discontinuities and complex anisotropic layering in the mantle lithosphere beneath the wyoming and superior provinces. *Journal of Geophysical Research: Solid Earth*, 121(9):6675–6697.

French, S., Lekic, V., and Romanowicz, B. (2013). Waveform tomography reveals channeled flow at the base of the oceanic asthenosphere. *Science*, 342(6155):227–230.

French, S. W. and Romanowicz, B. A. (2014). Whole-mantle radially anisotropic shear velocity structure from spectral-element waveform tomography. *Geophysical Journal International*, 199(3):1303–1327.

Grand, S. P. and Helmberger, D. V. (1984). Upper mantle shear structure of North America. *Geophysical Journal International*, 76(2):399–438.

Griffin, W., O'Reilly, S. Y., Doyle, B., Pearson, N., Coopersmith, H., Kivi, K., Malkovets, V., and Pokhilenko, N. (2004). Lithosphere mapping beneath the north american plate. *Lithos*, 77(1):873–922.

- Gung, Y., Panning, M., and Romanowicz, B. (2003). Global anisotropy and the thickness of continents. *Nature*, 422(6933):707–711.
- Heaman, L. and Kjarsgaard, B. (2000). Timing of eastern north american kimberlite magmatism: continental extension of the great meteor hotspot track? *Earth and Planetary Science Letters*, 178(3):253–268.
- Herrin, E. and Taggart, J. (1968). Regional variations in p travel times. *Bulletin of the Seismological Society of America*, 58(4):1325–1337.
- Hoffman, P. F. (1988). United plates of America, the birth of a craton: Early proterozoic assembly and growth of laurentia. *Annu. Rev. Earth Planet. Sci.*, 16(1):543–603.
- James, E. K., Dalton, C. A., and Gaherty, J. B. (2014). Rayleigh wave phase velocities in the atlantic upper mantle. *Geochemistry, Geophysics, Geosystems*, 15(11):4305–4324.
- Kennedy, W. (1964). The structural differentiation of africa in the pan-african ( $\pm 500$  my) tectonic episode. *Leeds Univ. Res. Inst. Afr. Geol. Annu. Rep*, 8:48–49.

King (2005). Archean cratons and mantle dynamics. *Earth and Planetary Science Letters*, 234(1-2):1–14.

Komatitsch, D. (2002). The spectral-element method, beowulf computing, and global seismology. *Science*, 298(5599):1737–1742.

Kustowski, B., Ekstrm, G., and Dziewoński, A. M. (2008). Anisotropic shear-wave velocity structure of the earth's mantle: A global model. *J. Geophys. Res.*, 113(B6).

Lee, C.-T. A., Luffi, P., and Chin, E. J. (2011). Building and destroying continental mantle. *Annu. Rev. Earth Planet. Sci.*, 39(1):59–90.

Lekić, V. and Romanowicz, B. (2011). Inferring upper-mantle structure by full waveform tomography with the spectral element method. *Geophysical Journal International*, 185(2):799–831.

Levin, V., Menke, W., and Park, J. (1999). Shear wave splitting in the appalachians and the urals- a case for multilayered anisotropy. *Journal of Geophysical Research*, 104(17):975–17.

Li, X.-D. and Romanowicz, B. (1995). Comparison of global waveform in-

- versions with and without considering cross-branch modal coupling. *Geophysical Journal International*, 121(3):695–709.
- Li, X.-D. and Romanowicz, B. (1996). Global mantle shear velocity model developed using nonlinear asymptotic coupling theory. *J. Geophys. Res.*, 101(B10):22245–22272.
- Marone, F., Gung, Y., and Romanowicz, B. (2007). Three-dimensional radial anisotropic structure of the north american upper mantle from inversion of surface waveform data. *Geophysical Journal International*, 171(1):206–222.
- Marone, F. and Romanowicz, B. (2007). The depth distribution of azimuthal anisotropy in the continental upper mantle. *Nature*, 447(7141):198–201.
- Masson, Y., Cupillard, P., Capdeville, Y., and Romanowicz, B. (2013). On the numerical implementation of time-reversal mirrors for tomographic imaging. *Geophysical Journal International*, 196(3):1580–1599.
- McKenzie, D., Daly, M. C., and Priestley, K. (2015). The lithospheric structure of pangea. *Geology*, 43(9):783–786.
- Mégnin, C. and Romanowicz, B. (2000). The three-dimensional shear velocity

- structure of the mantle from the inversion of body, surface and higher-mode waveforms. *Geophysical Journal International*, 143(3):709–728.
- Mochizuki, E. (1986). The free oscillations of an anisotropic and heterogeneous earth. *Geophysical Journal International*, 86(1):167–176.
- Mocquet, A. and Romanowicz, B. (1990). Three-dimensional structure of the upper mantle beneath the atlantic ocean inferred from longperiod rayleigh waves, ii. *Inversion. J. Geophys. Res.*, 95:6787–6798.
- Montagner, J.-P. and Anderson, D. L. (1989). Petrological constraints on seismic anisotropy. *Physics of the Earth and Planetary Interiors*, 54(1-2):82–105.
- Müller, R. D., Sdrolias, M., Gaina, C., and Roest, W. R. (2008). Age, spreading rates, and spreading asymmetry of the world’s ocean crust. *Geochemistry, Geophysics, Geosystems*, 9(4).
- Nance, R. D., Murphy, J. B., and Keppie, J. D. (2002). A cordilleran model for the evolution of avalonia. *Tectonophysics*, 352(1):11–31.
- Nettles, M. and Dziewoński, A. M. (2008). Radially anisotropic shear velocity

- structure of the upper mantle globally and beneath North America. *J. Geophys. Res.*, 113(B2).
- O'Brien, S., Wardle, R., and King, A. (1983). The avalon zone: a pan-african terrane in the appalachian orogen of canada. *Geological Journal*, 18(3):195–222.
- Panning, M. and Romanowicz, B. (2006). A three-dimensional radially anisotropic model of shear velocity in the whole mantle. *Geophysical Journal International*, 167(1):361–379.
- Pindell, J. L. and Kennan, L. (2009). Tectonic evolution of the gulf of mexico, caribbean and northern south america in the mantle reference frame: an update. *Geological Society, London, Special Publications*, 328(1):1–55.
- Poupinet, G. (1979). On the relation between p-wave travel time residuals and the age of continental plates. *Earth and Planetary Science Letters*, 43(1):149–161.
- Rader, E., Emry, E., Schmerr, N., Frost, D., Cheng, C., Menard, J., Yu, C.-Q., and Geist, D. (2015). Characterization and petrological constraints of the midlithospheric discontinuity. *Geochemistry, Geophysics, Geosystems*, 16(10):3484–3504.

Ritsema, J., Deuss, A., van Heijst, H. J., and Woodhouse, J. H. (2010). S40rts: a degree-40 shear-velocity model for the mantle from new Rayleigh wave dispersion, teleseismic traveltimes and normal-mode splitting function measurements. *Geophysical Journal International*, 184(3):1223–1236.

Romanowicz, B. (1987). Multiplet-multiplet coupling due to lateral heterogeneity: asymptotic effects on the amplitude and frequency of the earth's normal modes. *Geophysical Journal International*, 90(1):75–100.

Romanowicz, B. A. (1979). Seismic structure of the upper mantle beneath the United States by three-dimensional inversion of body wave arrival times. *Geophysical Journal International*, 57(2):479–506.

Romanowicz, B. A., Panning, M. P., Gung, Y., and Capdeville, Y. (2008). On the computation of long period seismograms in a 3-D earth using normal mode based approximations. *Geophysical Journal International*, 175(2):520–536.

Rondenay, S., Bostock, M. G., Hearn, T. M., White, D. J., and Ellis, R. M. (2000). Lithospheric assembly and modification of the se canadian shield: Abitibi-grenville teleseismic experiment. *Journal of Geophysical Research: Solid Earth*, 105(B6):13735–13754.

- Schaeffer, A. and Lebedev, S. (2014). Imaging the north american continent using waveform inversion of global and USArray data. *Earth and Planetary Science Letters*, 402:26–41.
- Schaeffer, A. J. and Lebedev, S. (2013). Global shear speed structure of the upper mantle and transition zone. *Geophysical Journal International*, 194(1):417–449.
- Shapiro, N. M. and Ritzwoller, M. H. (2002). Monte-Carlo inversion for a global shear-velocity model of the crust and upper mantle. *Geophysical Journal International*, 151(1):88–105.
- Silveira, G. and Stutzmann, E. (2002). Anisotropic tomography of the atlantic ocean. *Physics of the Earth and Planetary Interiors*, 132(4):237–248.
- Smith, D. L. (1982). Review of the tectonic history of the florida basement. *Tectonophysics*, 88(1-2):1–22.
- Su, W.-j., Woodward, R. L., and Dziewonski, A. M. (1994). Degree 12 model of shear velocity heterogeneity in the mantle. *Journal of Geophysical Research: Solid Earth*, 99(B4):6945–6980.

Tarantola, A. (2005). *Inverse problem theory and methods for model parameter estimation*. siam.

Tarantola, A. and Valette, B. (1982). Generalized nonlinear inverse problems solved using the least squares criterion. *Reviews of Geophysics*, 20(2):219–232.

Thomas, W. A. (2006). Tectonic inheritance at a continental margin. *GSA today*, 16(2):4–11.

Thybo, H. and Perchu, E. (1997). The seismic 8 discontinuity and partial melting in continental mantle. *Science*, 275(5306):1626–1629.

van der Lee, S. and Frederiksen, A. (2005). Surface wave tomography applied to the north american upper mantle. In *Seismic Earth: Array Analysis of Broadband Seismograms*, pages 67–80. Wiley-Blackwell.

van der Lee, S. and Nolet, G. (1997). Upper mantleSvelocity structure of North America. *Journal of Geophysical Research: Solid Earth*, 102(B10):22815–22838.

Wang, Z. and Dahlen, F. A. (1995). Spherical-spline parameteriza-

tion of three-dimensional earth models. *Geophysical Research Letters*, 22(22):3099–3102.

Woodhouse, J. H. and Dziewonski, A. M. (1984). Mapping the upper mantle: Three-dimensional modeling of earth structure by inversion of seismic waveforms. *Journal of Geophysical Research: Solid Earth*, 89(B7):5953–5986.

Yuan, H., French, S., Cupillard, P., and Romanowicz, B. (2014). Lithospheric expression of geological units in central and eastern North America from full waveform tomography. *Earth and Planetary Science Letters*, 402:176–186.

Yuan, H. and Romanowicz, B. (2010). Lithospheric layering in the north american craton. *Nature*, 466(7310):1063–1068.

Yuan, H., Romanowicz, B., Fischer, K. M., and Abt, D. (2011). 3-D shear wave radially and azimuthally anisotropic velocity model of the north american upper mantle. *Geophysical Journal International*, 184(3):1237–1260.

Yuan, Y. O. and Simons, F. J. (2014). Multiscale adjoint waveform-difference tomography using wavelets. *Geophysics*, 79(3):WA79–WA95.

Zhou, Y., Dahlen, F., Nolet, G., and Laske, G. (2005). Finite-frequency effects in global surface-wave tomography. *Geophysical Journal International*, 163(3):1087–1111.

Zhu, H., Bozdağ, E., and Tromp, J. (2015). Seismic structure of the european upper mantle based on adjoint tomography. *Geophysical Journal International*, 201(1):18–52.